

AE-NeRF: Augmenting Event-Based Neural Radiance Fields for Non-ideal Conditions and Larger Scenes

Chaoran Feng¹, Wangbo Yu^{1,2}, Xinhua Cheng¹, Zhenyu Tang¹, Junwu Zhang¹,
Li Yuan^{1,2*}, Yonghong Tian^{1,2*}

¹School of Electronic and Computer Engineering, Peking University, China

²Peng Cheng Laboratory, China

{chaoran.feng, wbyu, chengxinhua, zhenyutang, junwuzhang}@stu.pku.edu.cn, {yhtian, yuanli-ecce}@pku.edu.cn

Abstract

Compared to frame-based methods, computational neuromorphic imaging using event cameras offers significant advantages, such as minimal motion blur, enhanced temporal resolution, and high dynamic range. The multi-view consistency of Neural Radiance Fields combined with the unique benefits of event cameras, has spurred recent research into reconstructing NeRF from data captured by moving event cameras. While showing impressive performance, existing methods rely on ideal conditions with the availability of uniform and high-quality event sequences and accurate camera poses, and mainly focus on object level reconstruction, thus limiting their practical applications. In this work, we propose **AE-NeRF** to address the challenges of learning event-based NeRF from non-ideal conditions, including non-uniform event sequences, noisy poses, and various scales of scenes. Our method exploits the density of event streams and jointly learn a pose correction module with an event-based NeRF (e-NeRF) framework for robust 3D reconstruction from inaccurate camera poses. To generalize to larger scenes, we propose hierarchical event distillation with a proposal e-NeRF network and a vanilla e-NeRF network to resample and refine the reconstruction process. We further propose an event reconstruction loss and a temporal loss to improve the view consistency of the reconstructed scene. We established a comprehensive benchmark that includes large-scale scenes to simulate practical non-ideal conditions, incorporating both synthetic and challenging real-world event datasets. The experimental results show that our method achieves a new state-of-the-art in event-based 3D reconstruction.

Introduction

The rapid advancement of 3D reconstruction techniques has enabled the generation of high-fidelity novel views from camera captures of a scene, further fostering numerous downstream applications, including robotics (Zhang et al. 2023; Zhou et al. 2023; Kerr et al. 2022; Feng et al. 2024; Ma et al. 2024), 3D games (Xia et al. 2024; Condorelli and Luigini 2024), and scene understanding (Zhu et al. 2024a; Yu et al. 2024b). However, in environments with suboptimal lighting or rapid object motion, standard RGB cameras often struggle to capture enough scene information and may experience overexposure, underexposure, or motion blur, making

*Corresponding author.

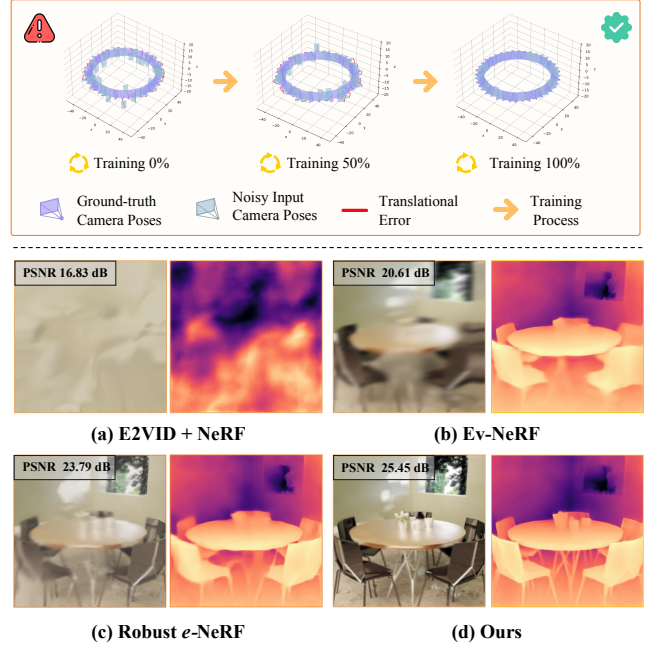


Figure 1: **Comparison of novel view synthesis (NVS) and pose correction using existing event-based methods.** The scene is captured by an event camera with 360-degree non-uniform motion and poses are estimated from COLMAP.

the captured images unsuitable for 3D scene reconstruction. In contrast, neuromorphic sensors, like event cameras (Gallego et al. 2020; Shao et al. 2023) which detect individual changes in brightness through a sequence of asynchronous events based on polarity rather than absolute intensities, provide significant advantages in such challenging situations due to their high dynamic range and temporal resolution.

Unfortunately, integrating event cameras into 3D reconstruction techniques remains challenging because these cameras capture relative brightness changes, which cannot be directly used to reconstruct scenes in alignment with human visual perception. Some methods combine depth map (Li et al. 2023) or standard cameras with event cameras to reconstruct 3D scenes, sacrificing the advantages of high temporal resolution offered by event cameras. Other approaches use stereo visual odometry (VO) (Zhou, Gallego, and Shen 2021) or SLAM (Gao et al. 2023) to address these

issues, but they can only reconstruct sparse 3D models like point clouds. The sparsity limits their broader applicability. Additionally, another method (Nehvi et al. 2021) initially represents objects as rough templates and then updates their deformations to align with events. However, these methods rely on template initialization, cannot address the impact of inaccurate poses, limited to specific object category scenes.

Neural Radiance Fields (NeRFs) (Mildenhall et al. 2020) has revolutionized the field of 3D scene reconstruction by learning neural 3D scene representation from dense image captures. It also inspired Event-based NeRF reconstruction methods, such as Ev-NeRF (Hwang, Kim, and Kim 2023), PAEv3d (Wang et al. 2024), Event-NeRF (Rudnev et al. 2023), and Robust *e*-NeRF (Low and Lee 2023). These methods bridge NeRF with event stream (or additional RGB frame) captured by event cameras for 3D reconstruction and are designed for handling scenes with extreme light condition or fast object motion. Nevertheless, these methods face fundamental challenges in non-ideal conditions that align with real-world scenarios. Firstly, these methods rely on ground truth poses (for synthetic data) or poses derived from complicated motion capture system (for real-world data) to train NeRF. This reliance is impractical in everyday settings, where the common approach for estimating poses from captured images is to use off-the-shelf Structure-from-Motion techniques, such as COLMAP (Schonberger and Frahm 2016). However, the accuracy of COLMAP rapidly degrades when handling low-quality RGB frames produced by event cameras, posing substantial challenges for the real applications of existing event-based NeRFs. Secondly, non-uniform camera movement is common in real-world scenarios, which can lead to inconsistencies in the density of the event stream captured by event camera, and further affect the reconstruction quality of event-based NeRFs. Additionally, existing methods mainly focus on reconstructing simple objects and suffer significant performance degradation when generalized to larger scenes. Figure 1 illustrates an example of using existing event-based NeRFs in a large scene with non-ideal conditions. It is evident that both E2VID+NeRF (Rebecq et al. 2019) and Ev-NeRF (Hwang, Kim, and Kim 2023) fail to reconstruct the 3D scene, while Robust-*e*-NeRF (Low and Lee 2023) also shows low fidelity.

In this work, to tackle the challenges of event-based NeRF reconstruction from non-ideal conditions and large scene, we make the following contributions:

- We propose **AE-NeRF**, a joint pose-NeRF training framework, which facilitates event-based NeRF reconstruction under various non-ideal conditions, particularly with inaccurate poses and uneven event density. As presented in Figure 1, it can effectively correct the inaccurate poses for better 3D reconstruction.
- We introduce a proposal network-based sampling strategy to address local minima optimization and large-scale generalization issues.
- We propose an event-based 3D reconstruction dataset with different complex scenes based on an improved version of ESIM (Rebecq et al. 2018), setting a benchmark for event-based NeRF reconstruction in large scenes.

Comprehensive experiments validates that our method significantly outperforms prior state-of-the-art on both synthetic and real-world datasets.

Related Work

3D Scene Representations

Prior research has investigated various methods for representing 3D scenes. Traditional approaches using explicit representations, such as point clouds (Qi et al. 2017; Achlioptas et al. 2018), meshes (Wang et al. 2018; Liu et al. 2020), and voxels (Byravan et al. 2023; Sitzmann et al. 2019), often struggle with fixed topology and limited quality in novel view synthesis. To address these issues, 3D Gaussian Splatting (3D-GS) (Kerbl et al. 2023) has been proposed, offering advantages in fast rendering speed and high-quality novel view synthesis. However, it requires point cloud initialization and does not effectively utilize the single-pixel characteristics of event stream, limiting the development of event data streams in 3D Gaussian Splatting.

NeRF (Mildenhall et al. 2020) has made significant strides by encoding continuous volumetric representations of shape and color within a multi-layer perceptron (MLP). This success has driven extensive research across computer vision, including large-scale scene reconstruction (Zhang et al. 2020; Barron et al. 2021; Tancik et al. 2022; Byravan et al. 2023), scene editing (Cheng et al. 2024), scene understanding (Zhi et al. 2021), SLAM (Zhu et al. 2024b; Rosinol, Leonard, and Carlone 2023), and generation (Tang et al. 2024; Yu et al. 2023a,b; Pang et al. 2024). For unbounded or large-scale scenes, methods like Mip-NeRF360 (Barron et al. 2022) have enabled scene-level reconstruction, while Block-NeRF (Tancik et al. 2022) and BungeeNeRF (Xi-angli et al. 2022) have extended this to city-scale reconstruction. The integration of single-pixel event data with NeRF through pixel ray marching leverages the high dynamic range and temporal resolution of event data, ensuring high geometric consistency and texture fidelity in the reconstructed results.

NeRF-based Reconstruction with Event Stream

In contrast to traditional 3D reconstruction methods, the application of event cameras in NeRF-based 3D reconstruction remains underexplored. Current NeRF techniques mainly focus on dense or sparse multi-view image reconstruction (Lu et al. 2024; Zou et al. 2024), often incorporating optical flow (Wang et al. 2023a), depth maps (Deng et al. 2022; Li et al. 2023), or point clouds (Truong et al. 2023; Jin et al. 2023). Early attempts to reconstruct NeRFs from event data include Ev-NeRF (Hwang, Kim, and Kim 2023), E-NeRF (Klenk et al. 2023), EventNeRF (Rudnev et al. 2023), and Robust *e*-NeRF (Low and Lee 2023). However, these approaches face limitations, such as reliance on precise camera trajectories in EventNeRF and the need for high-quality event streams in Ev-NeRF. In cases of inaccurate pose estimation or complex scenes, these methodologies struggle to maintain geometric consistency and texture fidelity.

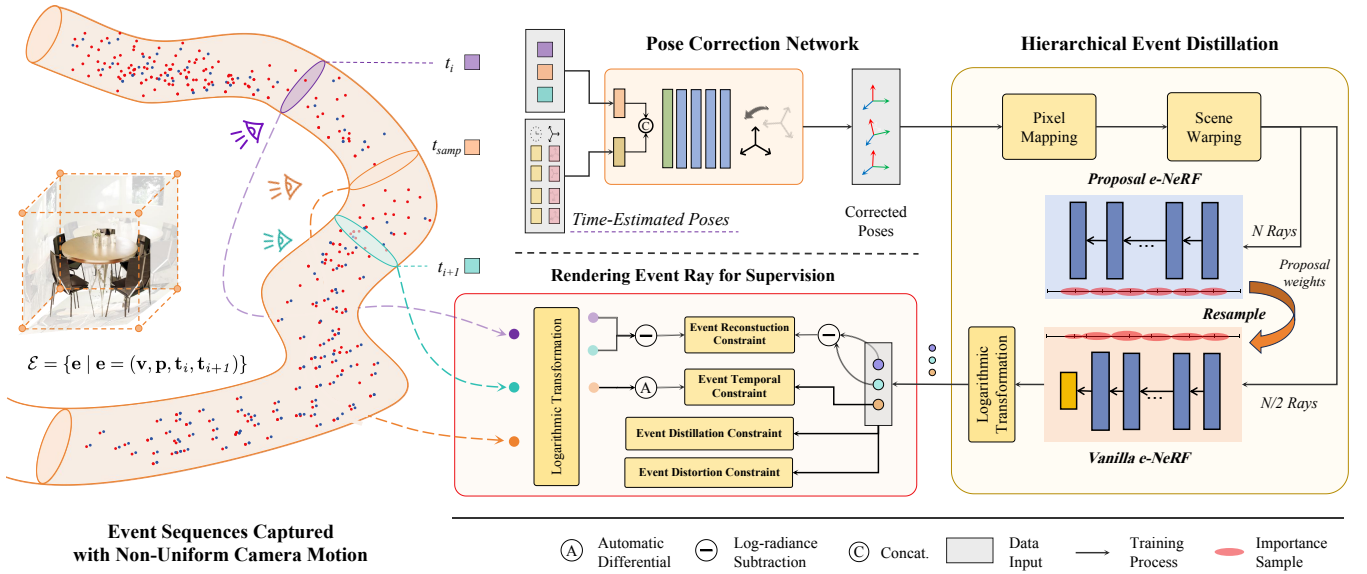


Figure 2: **Overview of AE-NeRF.** For each event e in the batch \mathcal{E} , randomly sampled from the raw sequences, we sample the timestamp t_{samp} between the previous timestamp t_i and the current timestamp t_{i+1} . We then use a pose correction network with timestamps-poses pairs to interpolate discrete poses with dense timestamps, yielding corrected poses at t_i , t_{i+1} , and t_{samp} . With these corrected poses, we process the event ray through scene warping and apply a two-stage e-NeRF to resample weights and distances, which infers the predicted log-radiance of pixel \mathbf{v} . The predicted event reconstruction difference and temporal gradient are then computed against the ground truth, utilizing distillation loss and distortion loss for regularization. Finally, a learning-based approach is employed for color correction to refine tone mapping.

Preliminary

Neural Radiance Fields

Our model draws its inspiration from the NeRF approach and the neural network $F_\theta(\cdot)$ processes a 3D coordinate $\mathbf{x}_i \in \mathbb{R}^3$ and a ray direction $\mathbf{d}_i \in \mathbb{S}^2$, outputting the density $\sigma_i \in \mathbb{R}$ and the emitted radiance $\mathbf{c}_i \in \mathbb{R}^3$:

$$F_\theta : (\gamma_x(\mathbf{x}_i), \gamma_d(\mathbf{d}_i)) \rightarrow (\sigma_i, \mathbf{c}_i), \quad (1)$$

Here, $\gamma(\cdot)$ is a sinusoidal positional encoding function capturing high-frequency spatial information. Rendering each pixel involves sampling N points along a ray $r(\mathbf{x}_0, \mathbf{d})$, where \mathbf{x}_0 is the ray's origin at the camera's focal point. The pixel color $\hat{\mathbf{L}}(r)$ is computed as:

$$\hat{\mathbf{L}}(r) = \sum_{i=1}^N w_i \mathbf{c}_i, \delta_i = \|\mathbf{x}_{i+1} - \mathbf{x}_i\|, \quad (2)$$

$$w_i = \exp\left(-\sum_{l=1}^{i-1} \sigma_l \delta_l\right) (1 - \exp(-\sigma_i \delta_i)).$$

The ray is rendered by sampling coarse distances t^c from a uniform distribution and sorted, followed by generating coarse weights w^c with an MLP. Fine distances t^f are then sampled from the histogram with t^c and w^c , and sorted:

$$\begin{aligned} t^c &\sim \mathcal{U}[t_n, t_f], & t^c &= \text{sort}(\{t^c\}), \\ t^f &\sim \text{hist}(t^c, w^c), & t^f &= \text{sort}(\{t^f\}). \end{aligned} \quad (3)$$

What's more, we adopt the normalization trick proposed in (Barron et al. 2022) to compute the ray distance s .

Event Generation Model

An event $e_k = (\mathbf{v}_k, p_k, t_k)$ represents a brightness change detected by an event camera at time t_k , with pixel location $\mathbf{v}_k = (x_k, y_k)$ and polarity $p_k \in \{-1, +1\}$. The polarity indicates positive or negative changes in logarithmic illumination, based on thresholds C^{+1} and C^{-1} . We adopt the event generation model from Robust e-NeRF (Low and Lee 2023), where an event camera captures log-radiance changes, producing an event stream \mathcal{E} :

$$\mathcal{E} = \{e \mid e = (\mathbf{v}, \mathbf{p}, t_i, t_{i+1})\}, \quad (4)$$

where each event records the current timestamp t_{i+1} and the previous timestamp t_i from the same pixel \mathbf{v} .

An event with polarity p is triggered when the log-radiance difference at a pixel reaches the contrast threshold C^p and the condition is expressed as:

$$\Delta \log \mathbf{L} := \log \mathbf{L}(\mathbf{v}, t_{i+1}) - \log \mathbf{L}(\mathbf{v}, t_i) = pC^p. \quad (5)$$

For color event cameras, \mathbf{L} represents the radiance of light after passing through the color filter in front of the pixel.

Methodology

This work addresses the challenge of novel view synthesis based on event neural implicit representations, in the non-uniform motion and unbounded-scene regime. Especially, we assume access to only discontinuous input views with noisy camera pose estimates in real-world scenarios.

To correct pose estimation and obtain continuous poses, we introduce a **pose correction network** $\psi(\cdot)$ using dense

timestamps as the main driving signal for the joint pose-NeRF training, thereby solving the challenge of imperfect poses. Moreover, to enhance eNeRF’s ability to represent unbounded scenes, we draw inspiration from (Barron et al. 2022) and utilize **hierarchical event distillation**. This approach trains two MLPs, with one resampling and predicting volumetric density and the other handling color estimation and image rendering, and thus encourages the learned scene geometry to be consistent across all viewpoints performance. Next, we propose and improve several normalization loss functions to **render event rays for supervision**, based on the event generation model. These functions generalize effectively to various real-world conditions, allowing joint optimization on randomly sampled event batches \mathcal{E}_{batch} to boost novel view rendering quality and further tackle the overfitting problem. Finally, instead of using gamma correction, we employ a learning-based approach for **color correction** to refine tone mapping. It restores photorealistic colors from relative light intensities, enhancing overall model performance. The overall pipeline is shown in Figure 2.

Pose Correction for Continuity

Since we are accustomed to capturing RGB images and event data streams with event cameras like DAVIS346 (Taverni 2020), it is inaccurate to directly estimate poses $\hat{P}_{\mathcal{E}}$ from RGB or gray images $I_{\mathcal{E}}$ using COLMAP with fixed sampled time $T_{\mathcal{E}}$. The timestamp of each event $t_i \in T_{\mathcal{E}}$ and image $I_i \in I_{\mathcal{E}}$ can form a time-image pair, serving as prior information. We achieve continuous time-pose mapping through the correction network $\psi(\cdot)$. The time-image pairs are embedded via a sparse head, and each timestamp t_i is also embedded. As shown in Figure 3 (a), this maps time to a helical axis representation $\psi := (t; T_{\mathcal{E}}, \hat{P}_{\mathcal{E}}) \rightarrow SE(3)$.

This pose correction network generates a continuous 6-DoF pose as a function of time, making it highly suitable for handling asynchronous events. Unlike other event-based NeRF approaches (Low and Lee 2023) that use trajectory interpolation or turntable poses, we address the joint problem of learning neural 3D representations and optimizing imperfect event poses, similar to BARF (Lin et al. 2021). The process can be formulated as follows:

$$\hat{P}_{corr}(t_i) = \psi(t_i, T_{\mathcal{E}}, \hat{P}_{\mathcal{E}}) \quad (6)$$

where $\hat{P}_{corr}(t_i)$ is the corrected pose at time t_i , $\psi(\cdot)$ is the correction module. This mapping transforms the time-image pairs into a continuous $SE(3)$ pose representation, ensuring accurate pose estimation for asynchronous event streams.

Hierarchical Event Distillation

The pose correction network favors a global and continuous solution that remains consistent across all training event sequences. However, the reconstructed scene often exhibits inconsistencies when viewed from novel viewpoints, due to the lack of fine sampling strategies for unbounded scenes during training. We propose a two-phase jointly optimized e-NeRF, designed to ensure that the learned geometry is consistent from any viewing direction.

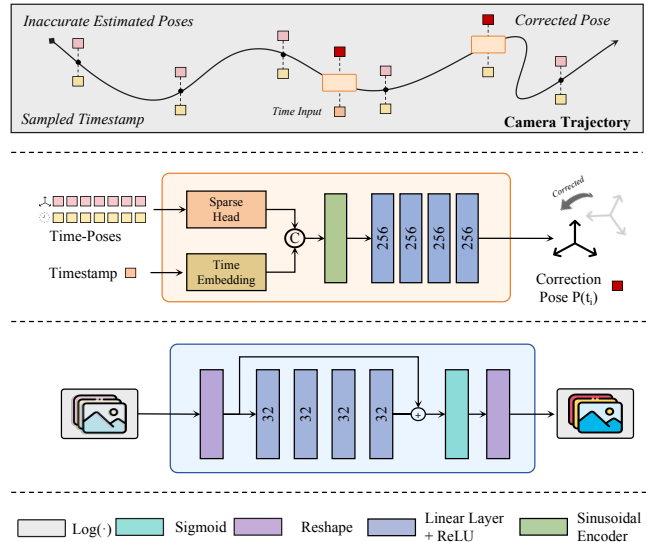


Figure 3: Framework of Pose Correction Network and Color Correction Network.

Scene warping It has been demonstrated that space warping functions, such as NDC warping (Mildenhall et al. 2020) and inverse sphere warping (Barron et al. 2023; Wang et al. 2023b), are effective for rendering unbounded scenes. We primarily use NDC warping for object-level scenes and employ uniform space warping $\mathcal{C}(\cdot)$ for unbounded scenes, as defined below:

$$\mathcal{C}(\mathbf{x}) = \begin{cases} \mathbf{x} & \|\mathbf{x}\| \leq 1 \\ \left(2 - \frac{1}{\|\mathbf{x}\|}\right) \left(\frac{\mathbf{x}}{\|\mathbf{x}\|}\right) & \|\mathbf{x}\| > 1 \end{cases} \quad (7)$$

Two-phase Jointly Optimized e-NeRF We use a larger vanilla e-NeRF alongside a smaller proposal e-NeRF, repeatedly evaluating and resampling numerous samples from the proposal e-NeRF. This approach allows our model to exhibit higher capacity than existing e-NeRF methods, with only slightly increased training costs. Utilizing a small MLP to model the proposal distribution does not compromise accuracy, indicating that distilling the NeRF MLP is simpler and more effective than view synthesis, as shown below:

$$F_{\varphi}^p(t, \hat{w}) \circ F_{\theta}^v(t, w) : (\gamma_x(\mathcal{C}(\mathbf{x})), \gamma_d(\mathbf{d})) \rightarrow (\sigma, \mathbf{c}) \quad (8)$$

In joint optimization process, a supervised method is needed to ensure consistency between the histograms produced by the proposal e-NeRF $F_{\varphi}^p(t, \hat{w})$ and the vanilla e-NeRF $F_{\theta}^v(t, w)$, as detailed in the following sections. Inspired by Mip-NeRF 360 (Barron et al. 2021), we adopt its histogram boundary function $\mathcal{B}(\cdot)$, which calculates the sum of proposal weights that overlap with interval T :

$$\mathcal{B}(\hat{t}, \hat{w}, T) = \sum_{j: T \cap \hat{T}_j \neq \emptyset} \hat{w}_j. \quad (9)$$

To maintain consistency between the two histograms, for all intervals T_i , w_i within (t, w) , the condition $w_i \leq \mathcal{B}(\hat{t}, \hat{w}, T_i)$ must be satisfied. This requirement resembles the additivity property of outer measures in measure theory.

This consistency ensures that the distributions between two-phase e-NeRFs remain relatively stable during resampling processes. With the boundary function, we can effectively constrain weights distribution of the proposal e-NeRF to match that of the vanilla e-NeRF, thus achieving a more efficient sampling process. It boosts the precision of sampling and the rendering quality during the training process.

Rendering Event Ray for Supervision

Overfitting directly to the training event streams leads to a compromised event neural radiance field that collapses towards the provided views, even when assuming perfect camera poses. With noisy and imperfect input poses, this issue is further exacerbated, making the L2 reconstruction loss unsuitable as the primary signal for joint pose-eNeRFs training. We apply several event regularization losses, to enforce learning a globally consistent 3D solution across the optimized scene geometry and camera poses.

Event Distillation Constraint. As mentioned earlier, we jointly optimize the proposal e-NeRF and vanilla e-NeRF, penalizing only the proposal weights that underestimate the distribution implied by the vanilla e-NeRF. Overestimation is expected since proposal weights are generally coarser and form an upper envelope over NeRF weights. This loss is similar to a half-quadratic version of the chi-squared histogram distance used in statistics and computer vision. We introduce the event threshold $\bar{C} = \frac{1}{2}(C^{-1} + C^{+1})$ to normalize this loss, further constraining the sampling distribution. Formally, the proposal loss is defined as:

$$\ell_p(t, w, \hat{t}, \hat{w}) = \sum_i \frac{1}{w_i} \max(0, \frac{w_i - \mathcal{B}(\hat{t}, \hat{w}, T_i)}{\bar{C}})^2 \quad (10)$$

Event Reconstruction Constraint. The main idea is aimed to use the log-radiance map $\Delta \log \hat{\mathbf{L}} := \log \hat{\mathbf{L}}(\mathbf{v}, t_{i+1}) - \log \hat{\mathbf{L}}(\mathbf{v}, t_i)$ rendered from the training viewpoints to match ground truth relative light intensity $\Delta \log \mathbf{L}$. Instead of L2 Reconstruction loss of NeRF, this difference is normalized using the event threshold for supervision, as follows:

$$\ell_r(e) = \frac{\text{MSE}(\Delta \log \hat{\mathbf{L}}, \Delta \log \mathbf{L})}{\bar{C}^2} \quad (11)$$

Note that when using a color event camera, $\hat{\mathbf{L}}$ refers to the single-channel rendered radiance, where the color channel is determined by the pixel’s color filter (Low and Lee 2023).

Event Temporal Constraint. To accurately capture the density of event streams under non-uniform motion, we compute the error between the predicted log-radiance gradient and the target log-radiance gradient, leveraging the high sampling rate of event cameras (Gallego et al. 2020). The predicted time gradient, obtained via auto-differentiation, is represented as $\mathcal{G}_{\text{pred}} = \frac{\partial}{\partial t} \log \mathbf{L}(\mathbf{v}, t)$, and is defined by:

$$\ell_g(e) = \left| \frac{\mathcal{G}_{\text{gt}} - \mathcal{G}_{\text{pred}}}{\mathcal{G}_{\text{gt}}} \right| \quad (12)$$

Here, the target gradient $\mathcal{G}_{\text{gt}} \approx \frac{pC^p}{t_{i+1} - t_i}$ is computed as a finite difference approximation, with sampling at t_{sam} .

Event Distortion Constraint. However, we notice that the depth consistency of the rendered results was not satisfactory, exhibiting some pathological depth issues. Inspired by total variance regularization (Michel et al. 2011), we adapted the smoothing from neighboring pixels to an integral over the distances between all points along the normalized ray. This integral is scaled by the weights assigned to each point by the vanilla e-NeRF, enforcing self-supervised smoothness and consistency of the ray weights:

$$\ell_d(s, w) = \sum_{i,j} w_i w_j \left| \frac{s_i + s_{i+1}}{2} - \frac{s_j + s_{j+1}}{2} \right| \quad (13)$$

In short, we use four normalized loss functions to supervise the model training with sampling a batch of events $\mathcal{E}_{\text{batch}}$ and formally, the total training loss \mathcal{L} is defined as:

$$\mathcal{L} = \frac{1}{|\mathcal{E}_{\text{batch}}|} \sum_{e \in \mathcal{E}_{\text{batch}}} (\alpha \ell_r + \beta \ell_g + \gamma \ell_p + \eta \ell_d) \quad (14)$$

Color Correction of Synthesized Views

Event cameras capture changes in log-radiance, leading to an offset in the predicted log-radiance $\log \hat{\mathbf{L}}$ from the NeRF reconstruction. Additionally, consistent color channel ambiguities, akin to unknown black levels and ISO in images, arise from spectral sensitivity differences between event and standard cameras. These can be corrected reconstruction with affine adjustments based on reference images, with parameters optimized via ordinary least squares.

However, this method tends to perform poorly in scenes with multiple objects or complex textures environments. To further improve this process, we adopt a learning-based approach. As shown in Figure 3(b), we employ a color correction network $\mathcal{F}(\cdot)$ to learn the correction process for RGB images of validation views in each scene and predict the color $\hat{\mathbf{c}}$ of test viewpoints from log-radiance intensity:

$$\hat{\mathbf{c}} = \mathcal{F}(\log \hat{\mathbf{L}}) \quad (15)$$

This approach allows for adaptive and precise tone mapping, capable of handling complex variations in the data.

Experiments

We utilize novel view synthesis (NVS) as a benchmark to demonstrate that our method can effectively reconstruct NeRF from event cameras, particularly in scenes with inaccurate pose estimation and sparse, noisy data caused by non-uniform motion. The NVS benchmark tests are conducted on both synthetic and real sequences. In addition, we perform ablation studies on pose optimization and losses to assess the impact of each component in our method.

Event Datasets. For synthetic scenes, similar to Ev-NeRF and Event NeRF, we utilize the synthetic dataset from NeRF (Mildenhall et al. 2020) and design additional synthetic event sequences, including event data streams, estimated poses from COLMAP, ground truth poses, and RGB images, using Blender (Community 2018). Our dataset includes four scenes inspired by Deblur-NeRF (Ma et al. 2022a) and four

Methods	Easy Settings			Hard Settings			Easy Settings			Hard Settings		
	PSNR \uparrow	SSIM \uparrow	LPIPS \downarrow	PSNR \uparrow	SSIM \uparrow	LPIPS \downarrow	PSNR \uparrow	SSIM \uparrow	LPIPS \downarrow	PSNR \uparrow	SSIM \uparrow	LPIPS \downarrow
E2VID+NeRF	18.92	.8328	.3167	18.92	.8328	.3167	15.60	.6212	.3298	15.60	.6212	.3298
Ev-NeRF	27.72	.9356	.0891	25.44	.8903	.1275	18.26	.7256	.2718	17.82	.6959	.2943
Event NeRF	26.81	.9183	.1007	24.92	.8783	.1377	17.99	.7048	.2881	17.68	.6933	.2996
Robust e-NeRF	<u>28.38</u>	<u>.9462</u>	.0578	<u>28.37</u>	<u>.9464</u>	.0578	21.48	.9033	.1204	21.41	.9028	.1207
Ours(w.o. ψ)	28.17	.9441	<u>.0541</u>	28.13	.9436	<u>.0550</u>	<u>22.83</u>	<u>.9105</u>	<u>.1169</u>	<u>22.79</u>	<u>.9098</u>	<u>.1172</u>
Ours(w. ψ)	28.96	.9512	.0478	28.90	.9503	.0485	24.28	.9324	.0975	24.23	.9324	.0981

Table 1: **Comparison of NVS for synthetic scenes.** Average performance is shown for object-level scenes in blue and for scenes from the proposed dataset in orange. The best and second-best results are highlighted in bold and underline.

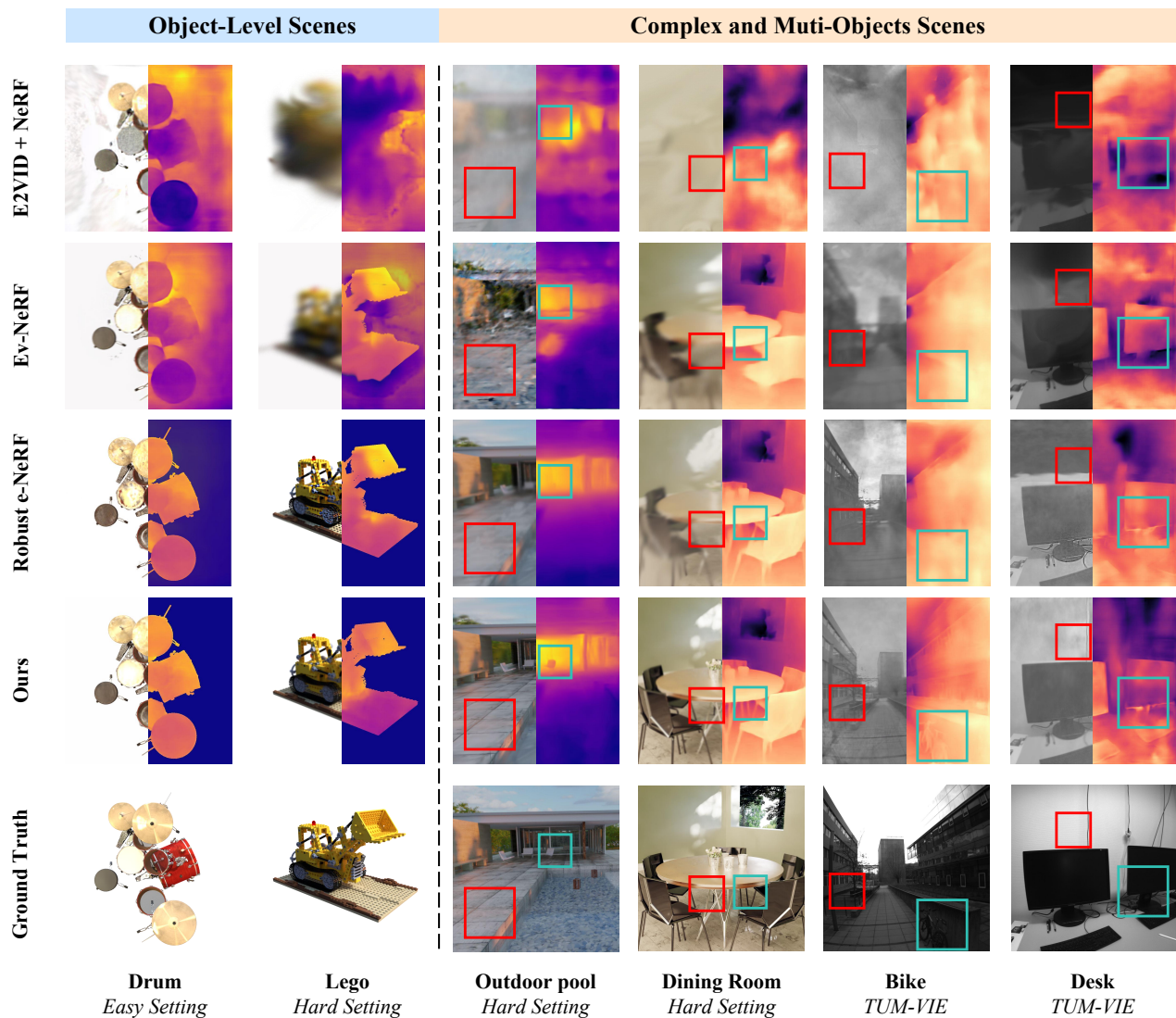


Figure 4: **Qualitative Comprison of Novel View Synthesis with AE-NeRF.**

additional custom scenes created with Blender and ESIM. These sequences are simulated in “Realistic Synthetic 360-degree” environments, which are rich in complexity and

texture, making them ideal for NVS evaluation. Following the approach of Robust e-NeRF (Low and Lee 2023), we classify the camera trajectories into simple and challenging

categories, detailed in the appendix. For real-world experiments, we use event sequences from the TUM-VIE dataset (Klenk et al. 2021), which primarily capture forward motion with a Prohesee Gen 4 event camera under linear and spiral movements, providing event data, ground truth poses, and grayscale images. To simulate real-world conditions, we also estimate images using COLMAP to obtain noisy poses.

Baseline Methods. We compare our method with a simple baseline method E2VID+NeRF which combines the well-known event-to-video reconstruction method E2VID with NeRF, and recent excellent works Ev-NeRF, Event NeRF and Robust *e*-NeRF.

Evaluation Metrics. The experimental results on both synthetic and real-world datasets are evaluated through the novel view synthesis task using quantitative metrics and qualitative comparisons of rendered images. Akin to previous studies, we use widely adopted evaluation metrics to compare synthesized images with corresponding ground truth images: PSNR, SSIM, and LPIPS to quantify the similarity between color-corrected synthesized novel views and target novel views. Moreover, we use rotation error (RE) and translation error (TE) to measure the accuracy of pose learning, further validating the model’s performance.

Methods	E2VID NeRF	Ev- NeRF	Event NeRF	Robust <i>e</i> -NeRF	Ours (w. ψ)
PSNR \uparrow	15.81	17.79	17.61	18.97	19.69
SSIM \uparrow	.6338	.7856	.7672	.8223	.8470
LPIPS \downarrow	.3072	.2138	.2203	.1964	.1882

Table 2: NVS Comparison the TUM-VIE dataset.

Evaluation on Synthetic Event Stream

We evaluate our method on the NeRF synthetic dataset and proposed dataset comprising eight scenes. As shown in Table 1, our method demonstrates notable improvement in large-scale scenes, though its impact is less pronounced in object-level scenes. It effectively preserves structural integrity, particularly at geometric discontinuities, such as the wheel in the “*lego*” scene and the ground in the “*outdoor pool*” scene. In contrast, the baseline method introduces significant background noise in the depth maps, whereas ours achieves clearer depth representations. Furthermore, our approach produces sharper renderings, while the benchmark results appear blurrier. Quantitative and qualitative comparisons are detailed in Table 1 and Figure 4.

Evaluation on Real Event Stream

We randomly select four scenes (*desk1*, *desk2*, *office*, *bike*) with different objects and materials for establishment. As stated in Figure 4, our approach faithfully reconstructs the main structures of objects even if there are some fog noises around them. In the scene of “*bike*”, the benchmark infers wrong geometries of the bike and leads to large variances in depth predictions. Moreover, the texture and depth map of wall in the scene of “*desk*” is wrongly rendered. In contrast,

ours maintains relatively clean shapes and sharper boundaries. And we additionally compute the metrics for the four scenes and the results are listed in Table 2.

Ablations Study

Pose Correction. We evaluate proposed model between the ground truth poses and corrected estimated poses in outdoor pool and diningroom with hard settings, as well as office and bike in real scenes, shown in Figure 1 and Table 3. It is evident that the pose correction network is significant in rectifying camera poses, particularly in complex environments where the camera motion is non-linear.

Scenes (w. ψ)	Synthetic Easy		Synthetic Hard		TUM-VIE	
	\checkmark	\times	\checkmark	\times	\checkmark	\times
RE \downarrow	0.085	0.086	0.127	0.881	0.431	1.283
TE \downarrow	0.867	0.872	1.472	3.751	1.676	4.487

Table 3: Ablation study of pose correction.

Loss Functions. We conclude the evaluation in the scenes same with pose correction ablation settings, in Table 4, the contribution of all the losses introduced above. Adding event time derivative for supervision from Eq.(12) improves PSNR by +3.39dB which is further increased when the event camera’s trajectory is irregular. Similarly, we evaluate on adding the event distortion loss in Eq.(13) and performance increases in this case, with a +0.57dB increase when adding this loss. The best performance is achieved when both are combined with an overall increase of +4.87dB in PSNR.

ℓ_p	ℓ_r	ℓ_g	ℓ_d	PSNR \uparrow	SSIM \uparrow	LPIPS \downarrow
\checkmark	\checkmark			19.80	.8356	.1811
\checkmark	\checkmark	\checkmark		23.19	.8852	.1494
\checkmark	\checkmark		\checkmark	20.37	.8413	.1775
\checkmark	\checkmark	\checkmark	\checkmark	24.67	.8971	.1337

Table 4: Ablation study of constrained loss.

Conclusion

This paper presents **AE-NeRF**, a novel approach designed to robustly reconstruct objects and scenes directly from moving event cameras under diverse real-world conditions. By leveraging the multi-view consistency of Neural Radiance Fields and the unique advantages of event cameras, our method addresses the challenges of inaccurate camera pose estimation and unbounded scene modeling through nonlinear scene parametrization, hierarchical distillation, and innovative regularizers. Comprehensive experiments on both synthetic and real-world datasets demonstrate that our method significantly outperforms state-of-the-art approaches and baseline benchmarks in terms of rendering quality and robustness. Our results highlight the effectiveness in enhancing novel view synthesis, even in complex environments. We will release our code and dataset to support further research and development in this field.

Acknowledgments

This work is supported in part by the Natural Science Foundation of China (No. 62332002, 62202014, 62425101, 62027804, 62088102).

References

- Achlioptas, P.; Diamanti, O.; Mitliagkas, I.; and Guibas, L. 2018. Learning representations and generative models for 3d point clouds. In *International conference on machine learning*, 40–49. PMLR.
- Barron, J. T.; Mildenhall, B.; Tancik, M.; Hedman, P.; Martin-Brualla, R.; and Srinivasan, P. P. 2021. Mip-NeRF: A Multiscale Representation for Anti-Aliasing Neural Radiance Fields. In *International Conference on Computer Vision (ICCV)*.
- Barron, J. T.; Mildenhall, B.; Verbin, D.; Srinivasan, P. P.; and Hedman, P. 2022. Mip-NeRF 360: Unbounded Anti-Aliased Neural Radiance Fields. In *Computer Vision and Pattern Recognition (CVPR)*.
- Barron, J. T.; Mildenhall, B.; Verbin, D.; Srinivasan, P. P.; and Hedman, P. 2023. Zip-NeRF: Anti-Aliased Grid-Based Neural Radiance Fields. In *International Conference on Computer Vision (ICCV)*.
- Byravan, A.; Humplik, J.; Hasenclever, L.; Brussee, A.; Nori, F.; Haarnoja, T.; Moran, B.; Bohez, S.; Sadeghi, F.; Vujatovic, B.; et al. 2023. Nerf2real: Sim2real transfer of vision-guided bipedal motion skills using neural radiance fields. In *2023 IEEE International Conference on Robotics and Automation (ICRA)*, 9362–9369. IEEE.
- Cheng, X.; Yang, T.; Wang, J.; Li, Y.; Zhang, L.; Zhang, J.; and Yuan, L. 2024. Progressive3D: Progressively Local Editing for Text-to-3D Content Creation with Complex Semantic Prompts. *arXiv:2310.11784*.
- Community, B. O. 2018. *Blender - a 3D modelling and rendering package*. Blender Foundation, Stichting Blender Foundation, Amsterdam.
- Condorelli, F.; and Luigini, A. 2024. Rapid and Low-Cost 3D Model Creation Using Nerf for Heritage Videogames Environments. In *Advances in Representation: New AI-and XR-Driven Transdisciplinarity*.
- Deng, K.; Liu, A.; Zhu, J.-Y.; and Ramanan, D. 2022. Depth-supervised NeRF: Fewer Views and Faster Training for Free. In *Computer Vision and Pattern Recognition (CVPR)*.
- Feng, K.; Ma, Y.; Wang, B.; Qi, C.; Chen, H.; Chen, Q.; and Wang, Z. 2024. Dit4edit: Diffusion transformer for image editing. *arXiv preprint arXiv:2411.03286*.
- Gallego, G.; Delbrück, T.; Orchard, G.; Bartolozzi, C.; Tabá, B.; Censi, A.; Leutenegger, S.; Davison, A. J.; Conrath, J.; Daniilidis, K.; et al. 2020. Event-based vision: A survey. *IEEE Trans. Pattern Analysis and Machine Intelligence (PAMI)*.
- Gao, L.; Su, H.; Gehrig, D.; Cannici, M.; Scaramuzza, D.; and Kneip, L. 2023. A 5-point minimal solver for event camera relative motion estimation. In *Proceedings of the IEEE/CVF International Conference on Computer Vision*, 8049–8059.
- Hidalgo-Carrió, J.; Gallego, G.; and Scaramuzza, D. 2022. Event-aided direct sparse odometry. In *Proceedings of the IEEE/CVF Conference on Computer Vision and Pattern Recognition*, 5781–5790.
- Hwang, I.; Kim, J.; and Kim, Y. M. 2023. Ev-nerf: Event based neural radiance field. In *Proceedings of the IEEE/CVF Winter Conference on Applications of Computer Vision*, 837–847.
- Jin, P.; Li, H.; Cheng, Z.; Li, K.; Ji, X.; Liu, C.; Yuan, L.; and Chen, J. 2023. Diffusionret: Generative text-video retrieval with diffusion model. In *Proceedings of the IEEE/CVF international conference on computer vision*, 2470–2481.
- Kerbl, B.; Kopanas, G.; Leimkühler, T.; and Drettakis, G. 2023. 3D Gaussian Splatting for Real-Time Radiance Field Rendering. *ACM Transactions on Graphics (TOG)*.
- Kerr, J.; Fu, L.; Huang, H.; Avigal, Y.; Tancik, M.; Ichnowski, J.; Kanazawa, A.; and Goldberg, K. 2022. Evo-nerf: Evolving nerf for sequential robot grasping of transparent objects. In *6th annual conference on robot learning*.
- Klenk, S.; Chui, J.; Demmel, N.; and Cremers, D. 2021. Tum-vie: The tum stereo visual-inertial event dataset. In *2021 IEEE/RSJ International Conference on Intelligent Robots and Systems (IROS)*, 8601–8608. IEEE.
- Klenk, S.; Koestler, L.; Scaramuzza, D.; and Cremers, D. 2023. E-nerf: Neural radiance fields from a moving event camera. *IEEE Robotics and Automation Letters*, 8(3): 1587–1594.
- Li, H.; Huang, J.; Jin, P.; Song, G.; Wu, Q.; and Chen, J. 2023. Weakly-supervised 3d spatial reasoning for text-based visual question answering. *IEEE Transactions on Image Processing*, 32: 3367–3382.
- Li, R.; Tancik, M.; and Kanazawa, A. 2022. Nerfacc: A general nerf acceleration toolbox. *arXiv preprint arXiv:2210.04847*.
- Lin, C.-H.; Ma, W.-C.; Torralba, A.; and Lucey, S. 2021. Barf: Bundle-adjusting neural radiance fields. In *Proceedings of the IEEE/CVF international conference on computer vision*, 5741–5751.
- Liu, S.; Li, T.; Chen, W.; and Li, H. 2020. A general differentiable mesh renderer for image-based 3D reasoning. *IEEE Transactions on Pattern Analysis and Machine Intelligence*, 44(1): 50–62.
- Low, W. F.; and Lee, G. H. 2023. Robust e-nerf: Nerf from sparse & noisy events under non-uniform motion. In *Proceedings of the IEEE/CVF International Conference on Computer Vision*, 18335–18346.
- Lu, Z.; Zheng, Q.; Shi, B.; and Jiang, X. 2024. Pano-NeRF: Synthesizing High Dynamic Range Novel Views with Geometry from Sparse Low Dynamic Range Panoramic Images. In *Proceedings of the AAAI Conference on Artificial Intelligence*, volume 38, 3927–3935.
- Ma, L.; Li, X.; Liao, J.; Zhang, Q.; Wang, X.; Wang, J.; and Sander, P. V. 2022a. Deblur-nerf: Neural radiance fields from blurry images. In *Proceedings of the IEEE/CVF Conference on Computer Vision and Pattern Recognition*, 12861–12870.

- Ma, L.; Li, X.; Liao, J.; Zhang, Q.; Wang, X.; Wang, J.; and Sander, P. V. 2022b. Deblur-NeRF: Neural Radiance Fields from Blurry Images. In *Computer Vision and Pattern Recognition (CVPR)*.
- Ma, Y.; He, Y.; Cun, X.; Wang, X.; Chen, S.; Li, X.; and Chen, Q. 2024. Follow your pose: Pose-guided text-to-video generation using pose-free videos. In *Proceedings of the AAAI Conference on Artificial Intelligence*, volume 38, 4117–4125.
- Michel, V.; Gramfort, A.; Varoquaux, G.; Eger, E.; and Thirion, B. 2011. Total Variation Regularization for fMRI-Based Prediction of Behavior. *IEEE Transactions on Medical Imaging*, 30(7): 1328–1340.
- Mildenhall, B.; Srinivasan, P. P.; Tancik, M.; Barron, J. T.; Ramamoorthi, R.; and Ng, R. 2020. NeRF: Representing Scenes as Neural Radiance Fields for View Synthesis. In *European Conference on Computer Vision (ECCV)*.
- Müller, T.; Evans, A.; Schied, C.; and Keller, A. 2022. Instant Neural Graphics Primitives with a Multiresolution Hash Encoding. *ACM Transactions on Graphics (TOG)*, 41(4): 102:1–102:15.
- Nehvi, J.; Golyanik, V.; Mueller, F.; Seidel, H.-P.; Elgharib, M.; and Theobalt, C. 2021. Differentiable event stream simulator for non-rigid 3d tracking. In *Proceedings of the IEEE/CVF Conference on Computer Vision and Pattern Recognition*, 1302–1311.
- Pang, Y.; Jin, P.; Yang, S.; Lin, B.; Zhu, B.; Tang, Z.; Chen, L.; Tay, F. E.; Lim, S.-N.; Yang, H.; et al. 2024. Next patch prediction for autoregressive visual generation. *arXiv preprint arXiv:2412.15321*.
- Paszke, A.; Gross, S.; Massa, F.; Lerer, A.; Bradbury, J.; Chanan, G.; Killeen, T.; Lin, Z.; Gimelshein, N.; Antiga, L.; et al. 2019. Pytorch: An Imperative Style, High-performance Deep Learning Library. *Advances in neural information processing systems*, 32.
- Qi, C. R.; Su, H.; Mo, K.; and Guibas, L. J. 2017. Pointnet: Deep learning on point sets for 3d classification and segmentation. In *Proceedings of the IEEE conference on computer vision and pattern recognition*, 652–660.
- Qi, Y.; Zhu, L.; Zhang, Y.; and Li, J. 2023. E2NeRF: Event Enhanced Neural Radiance Fields from Blurry Images. In *International Conference on Computer Vision (ICCV)*.
- Rebecq, H.; Gehrig, D.; and Scaramuzza, D. 2018. ESIM: an open event camera simulator. In *Conference on robot learning*, 969–982. PMLR.
- Rebecq, H.; Gehrig, D.; Scaramuzza, D.; and Feng, C. 2018. ESIM: an open event camera simulator. In *Conference on robot learning*, 969–982. PMLR.
- Rebecq, H.; Ranftl, R.; Koltun, V.; and Scaramuzza, D. 2019. High Speed and High Dynamic Range Video with an Event Camera. *IEEE Trans. Pattern Anal. Mach. Intell. (T-PAMI)*.
- Rosinol, A.; Leonard, J. J.; and Carlone, L. 2023. Nerf-slam: Real-time dense monocular slam with neural radiance fields. In *International Conference on Intelligent Robots and Systems (IROS)*.
- Rudnev, V.; Elgharib, M.; Theobalt, C.; and Golyanik, V. 2023. EventNeRF: Neural Radiance Fields from a Single Colour Event Camera. In *Computer Vision and Pattern Recognition (CVPR)*.
- Schonberger, J. L.; and Frahm, J.-M. 2016. Structure-from-motion Revisited. In *Computer Vision and Pattern Recognition (CVPR)*.
- Shao, Z.; Fang, X.; Li, Y.; Feng, C.; Shen, J.; and Xu, Q. 2023. EICIL: joint excitatory inhibitory cycle iteration learning for deep spiking neural networks. *Advances in Neural Information Processing Systems*, 36: 32117–32128.
- Sitzmann, V.; Thies, J.; Heide, F.; Nießner, M.; Wetzstein, G.; and Zollhofer, M. 2019. Deepvoxels: Learning persistent 3d feature embeddings. In *Proceedings of the IEEE/CVF Conference on Computer Vision and Pattern Recognition*, 2437–2446.
- Tancik, M.; Casser, V.; Yan, X.; Pradhan, S.; Mildenhall, B.; Srinivasan, P. P.; Barron, J. T.; and Kretzschmar, H. 2022. Block-nerf: Scalable large scene neural view synthesis. In *Proceedings of the IEEE/CVF Conference on Computer Vision and Pattern Recognition*, 8248–8258.
- Tang, Z.; Zhang, J.; Cheng, X.; Yu, W.; Feng, C.; Pang, Y.; Lin, B.; and Yuan, L. 2024. Cycle3d: High-quality and consistent image-to-3d generation via generation-reconstruction cycle. *arXiv preprint arXiv:2407.19548*.
- Taverni, G. 2020. *Applications of Silicon Retinas: From Neuroscience to Computer Vision*. Ph.D. thesis, Universität Zürich.
- Truong, P.; Rakotosaona, M.-J.; Manhardt, F.; and Tombari, F. 2023. Sparf: Neural radiance fields from sparse and noisy poses. In *Proceedings of the IEEE/CVF Conference on Computer Vision and Pattern Recognition*, 4190–4200.
- Wang, C.; MacDonald, L. E.; Jeni, L. A.; and Lucey, S. 2023a. Flow supervision for deformable nerf. In *Proceedings of the IEEE/CVF Conference on Computer Vision and Pattern Recognition*, 21128–21137.
- Wang, J.; He, J.; Zhang, Z.; and Xu, R. 2024. Physical Priors Augmented Event-Based 3D Reconstruction. *arXiv preprint arXiv:2401.17121*.
- Wang, N.; Zhang, Y.; Li, Z.; Fu, Y.; Liu, W.; and Jiang, Y.-G. 2018. Pixel2mesh: Generating 3d mesh models from single rgb images. In *Proceedings of the European conference on computer vision (ECCV)*, 52–67.
- Wang, P.; Liu, Y.; Chen, Z.; Liu, L.; Liu, Z.; Komura, T.; Theobalt, C.; and Wang, W. 2023b. F2-nerf: Fast neural radiance field training with free camera trajectories. In *Proceedings of the IEEE/CVF Conference on Computer Vision and Pattern Recognition*, 4150–4159.
- Xia, H.; Lin, Z.-H.; Ma, W.-C.; and Wang, S. 2024. Video2Game: Real-time Interactive Realistic and Browser-Compatible Environment from a Single Video. In *Computer Vision and Pattern Recognition (CVPR)*.
- Xiangli, Y.; Xu, L.; Pan, X.; Zhao, N.; Rao, A.; Theobalt, C.; Dai, B.; and Lin, D. 2022. Bungeenerf: Progressive neural radiance field for extreme multi-scale scene rendering. In *European conference on computer vision*, 106–122. Springer.

Yu, W.; Fan, Y.; Zhang, Y.; Wang, X.; Yin, F.; Bai, Y.; Cao, Y.-P.; Shan, Y.; Wu, Y.; Sun, Z.; et al. 2023a. Nofa: Nerf-based one-shot facial avatar reconstruction. In *ACM SIG-GRAPH 2023 Conference Proceedings*, 1–12.

Yu, W.; Feng, C.; Tang, J.; Jia, X.; Yuan, L.; and Tian, Y. 2024a. EvaGaussians: Event Stream Assisted Gaussian Splatting from Blurry Images. *arXiv preprint arXiv:2405.20224*.

Yu, W.; Xing, J.; Yuan, L.; Hu, W.; Li, X.; Huang, Z.; Gao, X.; Wong, T.-T.; Shan, Y.; and Tian, Y. 2024b. Viewcrafter: Taming video diffusion models for high-fidelity novel view synthesis. *arXiv preprint arXiv:2409.02048*.

Yu, W.; Yuan, L.; Cao, Y.-P.; Gao, X.; Li, X.; Quan, L.; Shan, Y.; and Tian, Y. 2023b. Hifi-123: Towards high-fidelity one image to 3d content generation. *arXiv preprint arXiv:2310.06744*.

Zhang, J.; Dai, L.; Meng, F.; Fan, Q.; Chen, X.; Xu, K.; and Wang, H. 2023. 3d-aware object goal navigation via simultaneous exploration and identification. In *Proceedings of the IEEE/CVF Conference on Computer Vision and Pattern Recognition*, 6672–6682.

Zhang, K.; Riegler, G.; Snavely, N.; and Koltun, V. 2020. Nerf++: Analyzing and improving neural radiance fields. *arXiv preprint arXiv:2010.07492*.

Zhi, S.; Laidlow, T.; Leutenegger, S.; and Davison, A. J. 2021. In-place scene labelling and understanding with implicit scene representation. In *Proceedings of the IEEE/CVF International Conference on Computer Vision*, 15838–15847.

Zhou, A.; Kim, M. J.; Wang, L.; Florence, P.; and Finn, C. 2023. Nerf in the palm of your hand: Corrective augmentation for robotics via novel-view synthesis. In *Computer Vision and Pattern Recognition (CVPR)*.

Zhou, Y.; Gallego, G.; and Shen, S. 2021. Event-Based Stereo Visual Odometry. *IEEE Transactions on Robotics*, 37(5): 1433–1450.

Zhu, C.; Li, K.; Ma, Y.; Tang, L.; Fang, C.; Chen, C.; Chen, Q.; and Li, X. 2024a. InstantSwap: Fast Customized Concept Swapping across Sharp Shape Differences. *arXiv preprint arXiv:2412.01197*.

Zhu, Z.; Peng, S.; Larsson, V.; Cui, Z.; Oswald, M. R.; Geiger, A.; and Pollefeys, M. 2024b. Nicer-slam: Neural implicit scene encoding for rgb slam. In *2024 International Conference on 3D Vision (3DV)*, 42–52. IEEE.

Zou, Y.; Li, X.; Jiang, Z.; and Liu, J. 2024. Enhancing Neural Radiance Fields with Adaptive Multi-Exposure Fusion: A Bilevel Optimization Approach for Novel View Synthesis. In *Proceedings of the AAAI Conference on Artificial Intelligence*, volume 38, 7882–7890.

Implementation Details

Datasets

Dataset Description Existing event synthetic datasets for scene reconstruction, such as those introduced by NeRF (Mildenhall et al. 2020) and E2NeRF (Qi et al. 2023), focus on object-level scenes. However, there is a notable lack of event synthetic datasets that cover large-scale scenes. Deblur-NeRF (Ma et al. 2022b) and EvaGaussians (Yu et al. 2024a) has introduced five larger-scale datasets with accompanying blender source files, but these datasets consist of rendered RGB images and do not include event sequences. To address this gap, we select four of the scenes from Deblur-NeRF and create four additional scenes ourselves, as shown in Figure 5. We generate synthetic event sequences for these scenes using ESIM (Rebecq, Gehrig, and Scaramuzza 2018), aiming to evaluate the model’s generalization ability in larger scenes.

In real-world scenarios, 3D event reconstruction methods such as PAEv3D (Wang et al. 2024) and Ev-NeRF (Hwang, Kim, and Kim 2023) have been limited to object-level scenes. It is due to the constraints imposed by the need for dense and perfect pose acquisition and the resolution limits of event cameras. Datasets like TUM-VIE (Klenk et al. 2021) and EDS (Hidalgo-Carrió, Gallego, and Scaramuzza 2022), which are used for event-based visual odometry tasks, provide perfect poses and high-quality event sequences. However, their scenes are not fully suitable for 3D reconstruction and novel view synthesis tasks. Additionally, due to the absence of a motion capture system for perfect and consistent poses, we are currently unable to capture real-world scene datasets. Consequently, we choose to quantitatively evaluate the model’s performance on real-world scenes using a subset of scenes from the TUM-VIE dataset.

Dataset Settings We conduct experiments on both synthetic and real-world scenes to evaluate our method. For the synthetic scenes, we use the object-level dataset (*chair, hot-dog, materials, ficus, mic, drum, lego*) from NeRF. Due to the constraints on scene size, we design and generate several synthetic event sequences using Blender (Community 2018) and ESIM (Rebecq, Gehrig, and Scaramuzza 2018), including four datasets from the Deblur-NeRF work including *outdoor pool, factory, cozyroom* and *tanabata* and four additional datasets we create (*Capsule, Dining Room, Garbage* and *Expressway*). These sequences are simulated in "Realistic Synthetic 360-degree" scenes, which feature complex environments and texture details. As shown in Table 5, we set the sampling rate for ground truth poses, normal images, and RGB images in Blender to 250Hz. We then use COLMAP to estimate the poses, thereby simulating real-world scenarios where camera poses are not error-free. The contrast thresholds in the ESIM simulator are set to $C^{+1} = C^{-1} = 0.25$ based on our empirical observations.

Inspired by Robust e-NeRF (Low and Lee 2023), we divide the camera trajectories into simple and challenging settings. In the simple setting, the camera moves at a uniform speed (with RGB images potentially containing some motion blur; we use slightly motion-blurred images for COLMAP and render a separate set of non-blurred im-

ages for validation and testing). In the challenging setting, the camera speed oscillates between $1/8\times$ and $8\times$ of the original speed at a frequency of 1Hz. Moreover, we use 100 surrounding viewpoints as the validation set and 100 randomly select novel viewpoints as the test set to evaluate the performance of our model.

Given the difficulty of obtaining absolutely accurate poses in real-world scenarios, our real-world experiments were conducted using event sequences from the TUM-VIE dataset. These sequences were captured indoors using a motion capture system to obtain forward-facing event camera data, ground truth poses, and gray images, under both linear and spiral camera movements, with a Prophesee Gen 4 event camera. We select four scenes (*mocap-desk1, mocap-desk2, office-maze, bike*) from this dataset. Additionally, we randomly select 30 novel views to evaluate the performance of our approach. Finally, although the task setting of PAEv3D dataset is not entirely aligned with our objectives, we still performed a comparison with their method. The results of this comparison are presented in the following section.

Settings	Value
Event \mathcal{E}	-
RGB images $I_{\mathcal{E}}$	250Hz
Normal images $N_{\mathcal{E}}$	250Hz
Ground Truth Poses $P_{\mathcal{E}}$	250Hz
Positive Threshold of ESIM C^{+1}	0.25
Negative Threshold of ESIM C^{-1}	0.25
Refractory Period	0 ns
Estimated Poses $\hat{P}_{\mathcal{E}}$	250Hz

Table 5: Detailed Settings of Proposed Synthetic Datasets

Model Architecture

AE-NeRF adopts Mip-NeRF360 (Barron et al. 2021) as the NeRF backbone due to its ability to produce high-quality reconstructions with relatively low memory consumption. Specifically, we utilize the implementation provided by the NerfAcc toolbox (Li, Tancik, and Kanazawa 2022). The parameters of the embedded Multi-Layer Perceptron (MLP) are initialized using the PyTorch-default method rather than Xavier initialization. Moreover, we replace all Rectified Linear Unit (ReLU) activations in the hidden layers with Soft-Plus, as it is infinitely differentiable, which facilitates the optimization of ℓ_g .

Initially, we employ the pose correction network $\psi(\cdot)$ to enhance the accuracy of the estimated poses, as outlined in Algorithm 1. The network $\psi(\cdot)$ refines time-estimated poses by integrating spatial and temporal information within a structured architecture. The network begins by processing the time-estimated poses ($\hat{P}_{\mathcal{E}}, T_{\mathcal{E}}$) through a sparse head, which consists of a linear layer that outputs a 256-

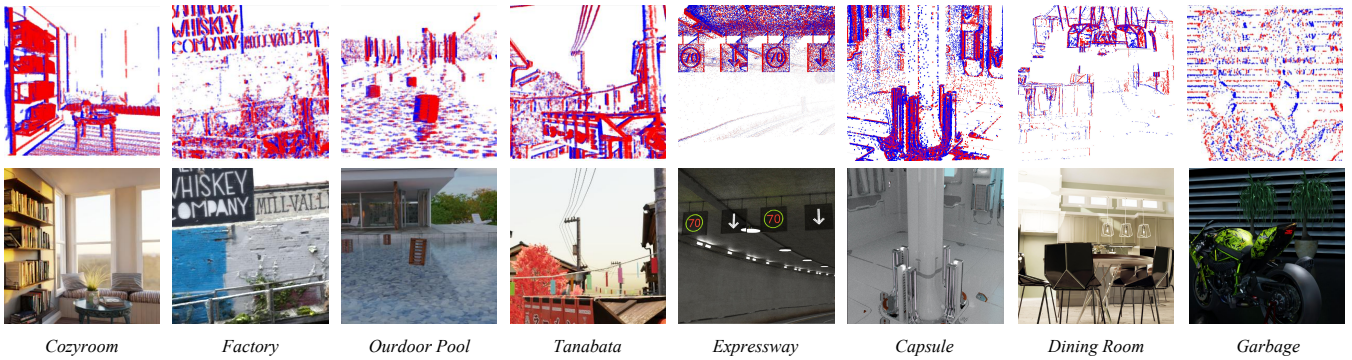


Figure 5: Proposed Synthetic Datasets of AE-NeRF.

dimensional pose embedding, followed by SoftPlus activation. Simultaneously, the specific time instance t_i is processed through another linear layer, also producing a 256-dimensional time embedding, activated by SoftPlus. These two embeddings are then combined into a single representation, which is further enhanced by a Sinusoidal Encoder that injects smooth temporal information. The enriched representation is subsequently passed through a sequence of four fully connected layers, each with 256 hidden units and SoftPlus activation, refining the feature representation. Finally, the network outputs the corrected pose $\hat{\mathbf{P}}_{corr}(t_i)$ via a linear transformation applied to the refined embedding. This architecture effectively integrates spatial and temporal cues, enabling precise pose correction in dynamic environments.

Then, we employ a *proposal e-NeRF* with four layers and 256 hidden units for the MLP layers, and a Vanilla e-NeRF with eight layers and 1024 hidden units for the MLP layers. Both configurations use SoftPlus for internal activation and density activation. We input samples for two stages of evaluation and resampling for each *proposal e-NeRF* to generate (\hat{t}, \hat{w}) , and then use half the number of samples to evaluate a single stage of *vanilla e-NeRF* to generate (t, w) .

Additionally, we add a small $\epsilon = 0.001$ to the positive raw radiance output from the NeRF model (i.e., $\hat{L} = \hat{L} + \epsilon$) to improve the numerical stability of the predicted log-radiance \hat{L} . This augmentation imposes a lower bound of ϵ on the radiance our method can model, ensuring $\hat{L} > \epsilon$.

For both synthetic and real scenes, we appropriately predefine the Axis-Aligned Bounding Box (AABB), as well as the near and far bounds of the back-projected rays used for volume rendering, for each scene.

Training

We implement our method using the code frameworks of PyTorch-Lightning, Robust e-NeRF (Low and Lee 2023), and NerfAcc (Li, Tancik, and Kanazawa 2022), and conducted the training on an Nvidia A6000 GPU. The training loss weights for all experiments are set as follows: $\lambda_\alpha = 1.00$, $\lambda_\beta = \lambda_\eta = 0.001$, and $\lambda_\gamma = 0.0025$. Following the recommendations from Instant-NGP (Müller et al. 2022) and Robust e-NeRF (Low and Lee 2023), we applied a weight decay of 10^{-6} to the MLP to mitigate overfitting. The

Algorithm 1: Pose Correction Network $\psi(\cdot)$

- 1: **Input:** Time-Estimated Poses $(\hat{\mathbf{P}}_\mathcal{E}, T_\mathcal{E})$, Time Input t_i
 - 2: **Output:** Corrected Pose $\hat{\mathbf{P}}_{corr}(t_i)$
 - 3: $P_{embedding} \leftarrow \text{ReLU}(\text{Linear}(\hat{\mathbf{P}}_\mathcal{E}, T_\mathcal{E}))$
 - 4: $T_{embedding} \leftarrow \text{ReLU}(\text{Linear}(t_i))$
 - 5: $C \leftarrow P_{embedding} + T_{embedding}$
 - 6: $C \leftarrow \text{Sinusoidal Encoder}(C)$
 - 7: **for** $i = 1$ to 4 **do**
 - 8: $C \leftarrow \text{ReLU}(\text{Linear}(C))$
 - 9: **end for**
 - 10: $\hat{\mathbf{P}}_{corr}(t_i) \leftarrow \text{Linear}(C)$
 - 11: **Return** $\hat{\mathbf{P}}_{corr}(t_i)$
-

model underwent 50,000 training iterations, with the learning rate reduced by a factor of 0.33 at 20,000, 30,000, and 36,000 iterations (i.e., at 50%, 75%, and 90% of the training process), as utilized in NerfAcc (Li, Tancik, and Kanazawa 2022). We employ the Adam optimizer with an initial learning rate of 0.01 and default hyperparameters provided by PyTorch (Paszke et al. 2019). The total time of training process takes 5 hours and 30 minutes.

During the joint optimization of the contrast threshold, a higher learning rate of 0.05 is assigned to its parameter to ensure rapid convergence. The event batch size is dynamically adjusted based on the average number of ray samples required to render a single pixel, akin to the approach used in Instant-NGP, to maximize GPU memory utilization. Specifically, each batch of events contained approximately 65,536 samples in total.

Additionally, for both the real scene target novel view poses and the synthetic scene poses without correction, we interpolate the unsynchronized constant-rate camera poses using Linear Interpolation (LERP) and Spherical Linear Interpolation (SLERP).

Additional Experiment Results

Visualization of Ray Sampling

Instant-NGP leverages an occupancy grid to efficiently cache scene density using a binarized voxel grid. During ray sampling, the grid is traversed with predetermined step sizes,

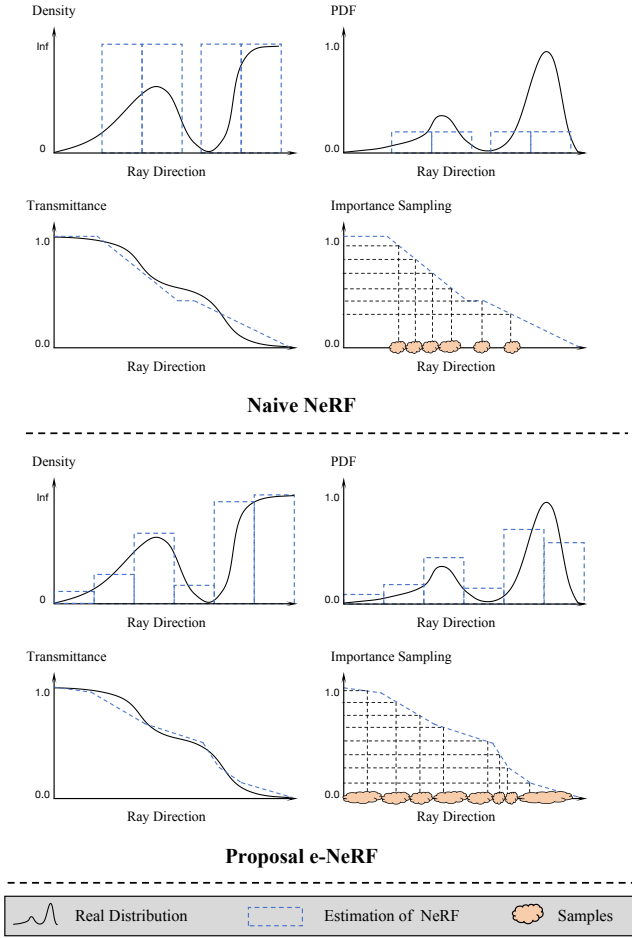


Figure 6: **Importance Sampling Comprison.**

allowing the algorithm to bypass empty regions by querying the voxel grid. Conceptually, the binarized voxel grid serves as an estimator of the radiance field, offering significantly faster readout. Formally, this estimator represents a binarized density distribution along the ray, governed by a conservative threshold $\hat{\sigma}$ and the corresponding piecewise linear transmittance $T(t_i)$:

$$\hat{\sigma}(t_i) = \mathbf{1}[\sigma(t_i) > \tau] \quad (16)$$

As a result, the piecewise constant probability density function (PDF) can be expressed as:

$$p(t_i) = \frac{\hat{\sigma}(t_i)}{\sum_{j=1}^n \hat{\sigma}(t_j)} \quad (17)$$

$$T(t_i) = 1 - \sum_{j=1}^{i-1} \frac{\hat{\sigma}(t_j)}{\sum_{j=1}^n \hat{\sigma}(t_j)} \quad (18)$$

However, this method exhibits suboptimal performance in complex scenes due to its inadequate sampling approach. To address this limitation, we propose an adaptive sampling strategy, employing a two-phase e-NeRF model that

enhances ray sampling efficiency and accelerates PDF construction.

Our method estimates the PDF along the ray using discrete samples directly. In the *vanilla e-NeRF*, the coarse MLP is trained with a volumetric rendering loss to output a set of densities. This process yields a piecewise constant PDF $\sigma(t_i)$ and a piecewise linear transmittance $T(t_i)$:

$$p(t_i) = \sigma(t_i) \exp(-\sigma(t_i) dt) \quad (19)$$

$$T(t_i) = \exp\left(-\sum_{j=1}^{i-1} \sigma(t_j) dt\right) \quad (20)$$

As illustrated in the Figure 6, our *proposed e-NeRF* model demonstrates superior performance compared to Instant-NGP in capturing fine-grained details. While there is a slight trade-off in overall performance, the expressiveness and consistency of our model are significantly improved.

Quantitative Analysis of Pose Correction

With noisy input poses, the problem of reconstruction becomes amplified, as shown in the quantitative results and ablation study in this paper. Thus, the approach of combining dense event data to correct pose significantly improves both continuity and accuracy, as demonstrated in Figure 7. In the optimization results for event sequences under *uniform camera motion*, both COLMAP estimations and **AE-NeRF** optimizations exhibit high accuracy and consistency. However, in scenarios involving *non-uniform camera motion*, COLMAP's pose estimates become significantly inaccurate due to motion ambiguity. In contrast, our method effectively corrects these erroneous poses, leading to superior reconstruction performance.

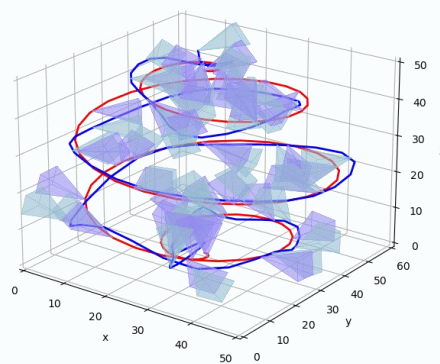
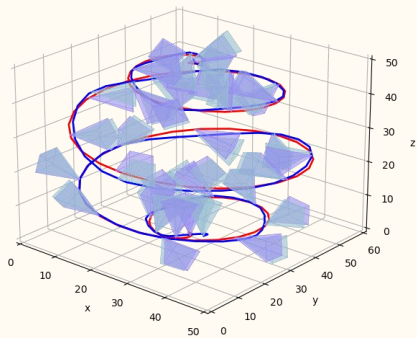
Qualitative Analysis of Losses

Figure 8 illustrates the impact of various loss functions on the *ficus* scene simulated under hard settings, the *capsule* scene and the *tanabata* scene sequences simulated under hard settings. It can be observed that with the inclusion of ℓ_g , the *ficus* scene exhibits clearer texture and geometric features. Meanwhile, the *capsule* and *tanabata* scenes demonstrate good reconstruction at close distances, albeit with the presence of floaters and depth inconsistencies at nearer distances. Furthermore, the results of the proposed approach combining ℓ_g and ℓ_d show a reduction in floaters and depth inconsistencies, along with sharper high-frequency details, particularly in challenging environments.

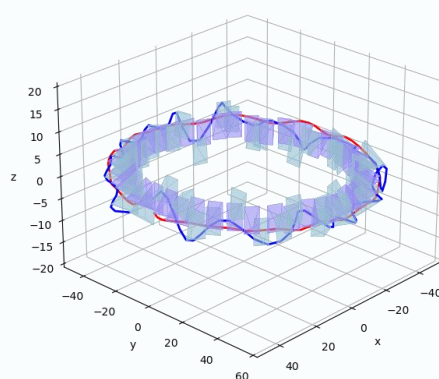
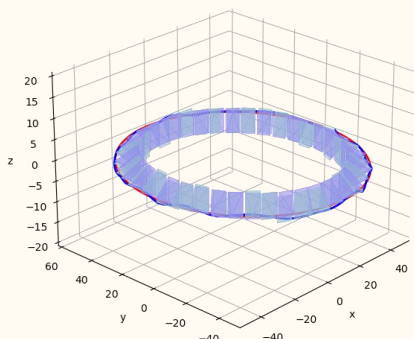
Quantitative Analysis in PAEv3D Datasets

In addition to the text experiments, we extend our evaluation by conducting further assessments on the dataset introduced by PAEv3D, which represents our latest advancement in event sequence-based 3D reconstruction. For this purpose, we selected three representative scenes (*bread*, *bounty*, and *telescope*) to carry out a comprehensive quantitative analysis, as summarized in Table 6. Although the scenarios presented in this dataset do not entirely correspond to the specific conditions and challenges of our task, our

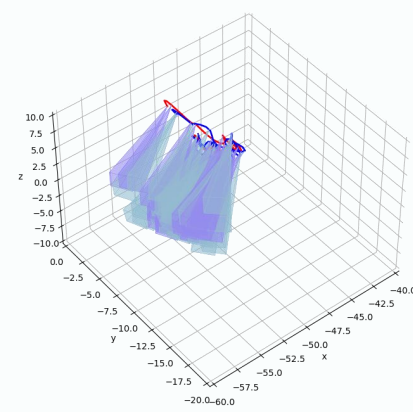
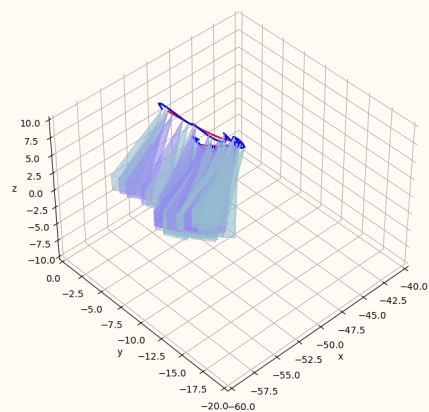
**Object-Level
Scenes**



**Proposed
Scenes**



**TUM-VIE
Scenes**



Easy Setting
Uniform Speed

Hard Setting
Non-Uniform Speed



Our Method
Poses



COLMAP
Poses



Our Method
Trajectory



COLMAP
Trajectory

Figure 7: Poses Optimization Comprison.

proposed method consistently demonstrates superior performance compared to existing approaches. This is particularly evident in the quantitative metrics, where our model exhibits

a notable improvement. Specifically, we observe an overall increase of +0.403 dB in PSNR, underscoring the model's enhanced capability to generalize across varied and complex

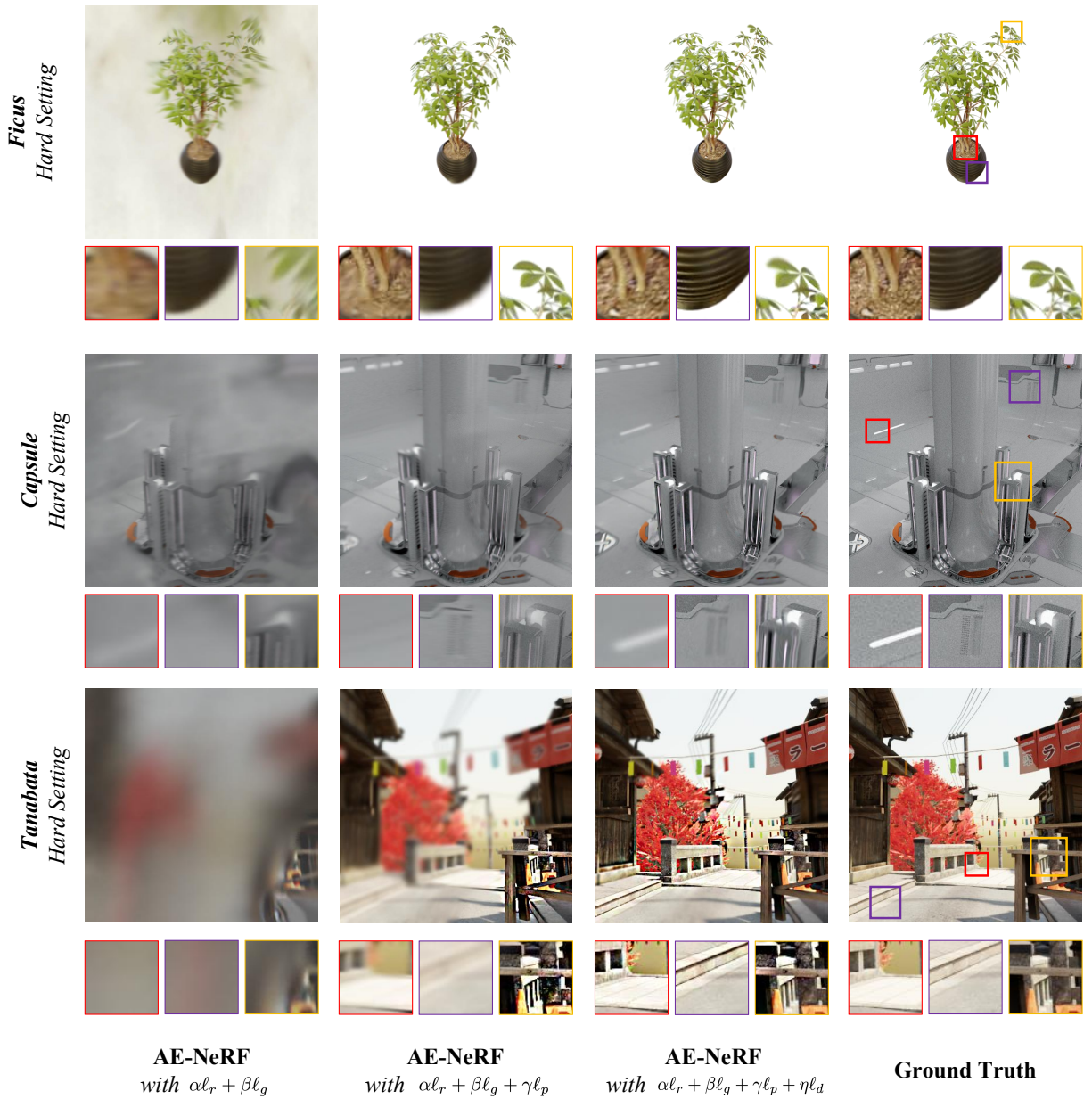


Figure 8: Synthesized novel views with and without losses.

	EventNeRF	PAEv3D	Robust e-NeRF	Ours
PSNR	20.273	<u>25.903</u>	25.812	26.306
SSIM	.9172	<u>.9401</u>	.9377	.9452
LPIPS	.2278	.0753	<u>.0718</u>	.0715

Table 6: **Quantitative Analysis of Novel View Synthesis in the PAEv3D Datasets.** We highlight the best-performing results with **bold**, and the second-performing result with underline.

environments. These results highlight the robust expressiveness of our approach, affirming its potential to effectively

handle diverse real-world scenarios, even those that deviate from the original task settings.

Limitation

Due to the absence of real-world datasets featuring accurate poses, non-uniform motion, and high-quality event sequences, our current approach is limited to reconstructing the event NeRF model using synthetic event sequences under complex conditions. Future research can explore more sophisticated 3D scene event reconstruction as challenging real-world datasets become available within the community.